Effect of confinement on the transition from two- to three-dimensional fast-rotating turbulent flows

Chandra Shekhar Lohani [1,*,†], Suraj Kumar Nayak [1,*,‡] and Kannabiran Seshasayanan [1,2]
[1]*Department of Physics, Indian Institute of Technology Kharagpur, 721302, India*
[2]*Department of Applied Mechanics and Biomedical Engineering, Indian Institute of Technology Madras, 600036, India*

(Received 23 August 2023; accepted 2 February 2024; published 11 March 2024)

We study the effect of confinement on the three-dimensional linear instability of fast-rotating two-dimensional turbulent flows. Using large-scale friction to model the effect of rigid boundaries at the top and bottom, we study the onset of three-dimensional perturbations on a rapidly rotating flow. The friction term is taken to affect both the evolution of the two-dimensional turbulent flow and the perturbations that evolve on top of it. Using direct numerical simulations, the threshold for the onset of three-dimensional perturbations is traced out as a function of the control parameters. As reported in the earlier work of Seshasayanan *et al.* [J. Fluid Mech. **901**, R5 (2020)], we find that the two different mechanisms, namely the centrifugal and parametric-type instabilities, are responsible for the destabilization across the wide range of parameters explored in this study. In the turbulent regime, we find that the large-scale friction term does not affect the threshold in the case of centrifugal instability, while in the case of parametric instability, the large-scale friction makes the flow stable for a wider range of parameters. For the parametric instability, the length scale of the unstable mode is found to scale as the inverse square root of the rotation rate and the growth rate of the unstable mode is found to be correlated with the minimum of the determinant of the strain rate tensor of the underlying two-dimensional turbulent flow, showing resemblance with elliptical type instabilities. Results from the turbulent flow are then compared with the oscillatory Kolmogorov flow, which also undergoes parametric instability resulting into inertial waves. The dependence of the threshold on the aspect ratio of the system is discussed for both the turbulent and the oscillating Kolmogorov flows.

DOI: 10.1103/PhysRevFluids.9.034604

I. INTRODUCTION

Many naturally occurring geophysical and astrophysical flows are turbulent and are subject to global rotation [1–3], with rotation leading to the formation of large-scale coherent motions. Vertical confinement can also help in the formation of coherent structures with thin layer flows becoming effectively two-dimensional, see Ref. [4] and references therein. In the presence of rapid rotation and when the forcing is invariant along the axis of rotation, it is known that the flow bidimensionalizes and the resulting flow is referred to as a geostrophic flow due to the dominant balance between the pressure term and the Coriolis term [5–8]. While in the case of forcing which is three-dimensional, the flow exhibits strong three-dimensional fluctuations along with columnar

*These authors contributed equally to this work.
†cslohani25@gmail.com
‡surajkumarnayak96@gmail.com

 ©2024 American Physical Society

structures in the large rotation limit, see Refs. [9,10]. Thus, one finds that the forcing plays an important role in determining the state of turbulent flow in the fast-rotation limit. Here the coupling between the geostrophic flow and inertial waves becomes weaker as the rotation rate increases.

Under weak or no global rotation a three-dimensional turbulent flow cascades the injected energy to smaller length scales leading to a forward energy cascade. As one increases the rotation rate with Rossby numbers $\mathrm{Ro} \lesssim 1$, some amount of the injected energy goes to large-scales in the form of an inverse energy cascade, which leads to the formation of coherent structures. Using the root-mean-square (r.m.s.) velocity $U = \langle |\mathbf{u}|^2 \rangle^{1/2}$, length scale L, the advective timescale L/U and the rotation rate along z direction Ω, we can define the nondimensional parameter, the Rossby number $(\mathrm{Ro}) = U/(2\Omega L)$, where $\langle \cdot \rangle$ denotes spatial and temporal averaging. From zero rotation as the rotation rate increases we see the onset of two-dimensionalization from a three-dimensional turbulent flow, which has been studied by Refs. [9,11,12]. In some studies [13,14], such a transition is found to occur through a critical point in the Rossby number, beyond which a dual cascade of energy exists. Such change in the direction of the cascade has been studied in various contexts, see Ref. [15], and in certain situations displays phenomena similar to critical phase transitions, see Refs. [16,17].

As the rotation rate is increased further $\mathrm{Ro} \ll 1$, it was shown in Ref. [18] that at long times the flow reaches a state of two-dimensional turbulence, where three-dimensional fluctuations decay to zero. This result was shown using the method of bounds which leads to an estimate for the threshold $\mathrm{Ro}_c \sim \mathrm{Re}^{-6}$. $\mathrm{Re} = UL/\nu$ is Reynolds number where ν is the kinematic viscosity of the fluid. Later, this threshold problem was posed as a linear instability of rapidly rotating two-dimensional turbulent flow in Ref. [19]. Using numerical simulations, it was found that the threshold scales as $\mathrm{Ro}_c \sim \mathrm{Re}^{-1}$ in the limit of very large Re, below this threshold, infinitesimal three-dimensional perturbations decay to zero. The scaling $\mathrm{Ro}_c \sim \mathrm{Re}^{-1}$ results from a parametric instability of large-scale two-dimensional vortices in the large Re limit. While for lower values of Re, the centrifugal instability gave rise to a threshold $\mathrm{Ro}_c \sim \mathrm{Re}^{0}$. It remains to be seen whether the threshold $\mathrm{Ro}_c \sim \mathrm{Re}^{-1}$ holds in the case of nonlinear stability of the rapidly rotating turbulent flow.

While the results of Ref. [19] hold for periodic or free-slip boundary conditions, the influence of solid boundaries on the threshold is unknown, while in experiments and naturally occurring flows, two-dimensionalization is observed in the interior far from the boundaries, see Refs. [6,20,21]. Near the boundaries, Ekman layers develop where the balance between the viscous force and the Coriolis force leads to the formation of a thin boundary layer having thickness $\mathcal{O}(\sqrt{\nu/\Omega})$. To study the problem numerically at large Reynolds number Re and low Rossby number Ro, one has to perform large-scale simulations that resolve the boundary layers and also capture the temporal evolution of the fast inertial waves. An alternate approach is to model the rigid boundaries as an additional friction term, such an approach has been used in many different contexts from modeling laboratory flows to geophysical flows. Large-scale friction has also been used widely in quasi-two-dimensional flows where the friction parameter arises from the confinement effects. In geophysical flows, Ekman layers are widely observed at both free surface and rigid bottom boundaries leading to a dissipative effect on the large-scale flows. While linear friction is found to work well when the boundary layers are laminar, quadratic friction is used to model the turbulent boundary layers [22]. In rotating flows, Ekman friction in the form of a linear drag has been used in both numerical simulations [23] and experiments [24] to model the flow between boundaries. In this work, we consider the case of linear friction as a model to capture the effects of solid boundaries. We aim to understand the effect of large-scale friction on the instability threshold and explore further the mechanisms of the instability of rapidly rotating two-dimensional turbulent flows. The coefficient of friction in the Ekman friction term is found in many situations using decay experiments [22,25,26] and in general, it can depend on the Reynolds number, the roughness of the boundaries, aspect ratio, etc., and an expression for the large-scale friction coefficient in terms of these parameters is not known. To avoid modeling the exact form of the large-scale friction term in terms of the other parameters of the system, we study the threshold problem for a wide range of large-scale friction parameters.

The question of two-dimensionalization is also posed in the limit of elongated boxes since the timescales of inertial waves can become comparable to the turnover timescale. In such systems,

the flow can go to quasi-two-dimensional turbulent flows or possibly lead to the disintegration of large-scale vortices into inertial waves. Recent works [14,27] have explored this limit to understand the formation or disintegration of two-dimensional vortices in elongated domains. The frequency of the slowest inertial waves is given by $\omega_f = 2\Omega L/H$ where H is the height of the domain parallel to the rotation axis, and L is the typical size of the domain in the plane perpendicular to the rotation axis. An estimate for the threshold for the cross-over from coherent vortical structures to inertial waves is given by balancing the two timescales leading to $\mathrm{Ro} \times (H/L) \sim O(1)$. The work by Ref. [14] showed that such a scaling could predict when a three-dimensional turbulent flow begins to cascade energy to large scales as the rotation rate increases from zero. While the work by Ref. [27] looked into the stability of a pair of elongated vortices, [28] used the point vortex model of localised 3D perturbations on top of quasi-two-dimensional turbulence to understand three-dimensional instabilities. This study examines the scaling associated with the onset of three-dimensional perturbations on top of rapidly rotating two-dimensional turbulence in the large Reynolds limit.

The present work looks into the effect of large-scale friction on the threshold of three-dimensional instability and the underlying instability mechanisms for different domain sizes using Direct Numerical Simulations (DNS). Section II explains the mathematical setup for the system considered and the numerical method used to solve the system of equations. Section III describes the dependence of the critical Rossby number threshold on the large-scale dissipation rate for different values of the Reynolds number and aspect ratio. This section also elaborates further on the instability length scales for the parametric instability and the correlation between the rate of strain tensor of the two-dimensional turbulent flow and the growth of the three-dimensional perturbations. Section IV describes the threshold using the oscillating Kolmogorov as a model for the turbulent flow. The differences between the oscillating Kolmogorov flow and the turbulent flow are discussed. In the end, Sec. V summarizes the results and limitations of the work.

II. MATHEMATICAL FORMULATION

We consider an incompressible fluid in a domain of dimensions $[0, L] \times [0, L] \times [0, H]$ with the system subject to a global rotation rate Ω along the vertical direction $\mathbf{e}_z$ (Fig. 10). The Navier Stokes equation in the rotating frame can be written as

$$\frac{\partial \mathbf{u}}{\partial t} + (\mathbf{u}\cdot\nabla)\mathbf{u} = -\frac{1}{\rho}\nabla p + \nu\nabla^2\mathbf{u} + 2\Omega\mathbf{u}\times\mathbf{e}_z + \mathbf{f}, \tag{1}$$

$$\nabla\cdot\mathbf{u} = 0, \tag{2}$$

where $\mathbf{u}(\mathbf{x}, t) = u\,\mathbf{e}_x + v\,\mathbf{e}_y + w\mathbf{e}_z$ is the velocity field and $p(\mathbf{x}, t)$ is the pressure. The forcing $\mathbf{f}$ is taken to be the Kolmogorov forcing along the x direction, $\mathbf{f} = f_0\cos(8\pi y/L)\mathbf{e}_x$ where f_0 is the amplitude of the forcing. It is noted that the forcing considered here is invariant along the axis of rotation which is the z direction.

In the limit of a very large rotation rate, the velocity field becomes invariant along the vertical direction effectively becoming a two-dimensional flow. We are interested in finding the linear threshold where three-dimensional perturbations grow exponentially on top of the turbulent two-dimensional flow. In the low Ro limit, we write the total velocity field $\mathbf{u}$ and the pressure field p as

$$\mathbf{u}(\mathbf{x}, t) = \mathbf{u_{2D}}(\mathbf{x}, \mathrm{t}) + \mathrm{Ro}\ \mathbf{u_{3D}}(\mathbf{x}, \mathrm{t}) + \mathrm{O}(\mathrm{Ro}^2), \tag{3}$$

$$p(\mathbf{x}, t) = \mathrm{Ro}^{-1}p_G(\mathbf{x}, t) + p_{2\mathrm{D}}(\mathbf{x}, t) + \mathrm{Ro}\ p_{3\mathrm{D}}(\mathbf{x}, t) + O(\mathrm{Ro}^2). \tag{4}$$

Here $\mathbf{u_{2D}}$ denotes the dominant component of the velocity field which is two-dimensional in the interior of the fluid, except near the boundaries where the flow depends on the z direction. In what follows, we model the effect of boundary layers as an effective linear dissipation term, the details of the approximations taken in the derivation of such a linear friction coefficient are given in the

Appendix. Thus, we only concentrate on the quantities in the expansion given in Eqs. (3) and (4), as they denote the velocity and pressure components in the interior of the fluid far from the boundary layers.

Substituting the above equation into Eqs. (1) and (2), we get the balance between pressure term ∇p_G and the Coriolis force $\mathbf{u_{2D}} \times \mathbf{e}_z$ at order $O(\mathrm{Ro}^{-1})$. At the next order in Ro^0, we get the evolution equation for the large-scale two-dimensional velocity field, denoting the dominant component of the velocity field. The resulting equation with the addition of the frictional term reads as (see the Appendix),

$$\frac{\partial \mathbf{u_{2D}}}{\partial t} + (\mathbf{u_{2D}}.\nabla)\mathbf{u_{2D}} = -\frac{1}{\rho}\nabla p_{2\mathrm{D}} + \nu\nabla^2\mathbf{u_{2D}} - \mu\,\mathbf{u_{2D}} + \mathbf{f}, \tag{5}$$

where μ denotes the large-scale friction which models the dissipation effect of the top and bottom boundary layers [4,29,30]. We denote Rh as the large-scale Reynolds number defined as $\mathrm{Rh} = U/(\mu L)$.

In the next order, we get the evolution equation for the 3D perturbations that evolve on the 2D turbulent base flow. The equation for 3D perturbation takes the form (see the Appendix):

$$\frac{\partial \mathbf{u_{3D}}}{\partial t} + (\mathbf{u_{2D}} \cdot \nabla)\mathbf{u_{3D}} + (\mathbf{u_{3D}} \cdot \nabla)\mathbf{u_{2D}} = -\frac{1}{\rho}\nabla p_{3D} + \nu\nabla^2\mathbf{u_{3D}} + 2\Omega(\mathbf{u_{3D}} \times \mathbf{e}_z) - \mu\mathbf{u_{3D}}. \tag{6}$$

Since $\mathbf{u_{2D}}$ is independent of vertical coordinates in the interior of the flow, the three-dimensional perturbations can be decomposed into vertical Fourier modes with each mode (q) evolving independently in the linear stability problem. The perturbation form can be written as

$$\mathbf{u_{3D}}(x, y, z, t) = \widehat{\mathbf{u}}_{\mathbf{3D}}(x, y, t)e^{iqz} + \widehat{\mathbf{u}}^*_{\mathbf{3D}}(x, y, t)e^{-iqz}. \tag{7}$$

Similarly, we can write pressure as

$$p_{3\mathrm{D}}(x, y, z, t) = \widehat{p}_{3\mathrm{D}}(x, y, t)e^{iqz} + \widehat{p}^*_{3\mathrm{D}}(x, y, t)e^{-iqz}. \tag{8}$$

For the perturbations fields $\widehat{\mathbf{u}}_{\mathbf{3D}}(x, y, t)$, we assume that away from the boundary layers the fields obey stress-free boundary conditions, thus the vertical wave number q is related to the height H by the relation $q = \pi/H$. We take periodic boundary conditions along the lateral directions x, y for all quantities. Substituting the above expression for the unstable mode into the governing equation (6), we end up with the following:

$$\begin{aligned}\frac{\partial \widehat{\mathbf{u}}_{\mathbf{3D}}}{\partial t} &+ (\mathbf{u_{2D}} \cdot \nabla_\perp)\widehat{\mathbf{u}}_{\mathbf{3D}} + (\widehat{\mathbf{u}}_{\mathbf{3D}} \cdot \nabla_\perp)\mathbf{u_{2D}} \\ &= -\frac{1}{\rho}(\nabla_\perp + iq\mathbf{e}_z)\widehat{p}_{3\mathrm{D}} + \nu(\nabla^2_\perp - q^2)\widehat{\mathbf{u}}_{\mathbf{3D}} + 2\Omega(\widehat{\mathbf{u}}_{\mathbf{3D}} \times \mathbf{e}_z) - \mu\widehat{\mathbf{u}}_{\mathbf{3D}},\end{aligned} \tag{9}$$

where $\nabla_\perp \equiv \frac{\partial}{\partial x}\mathbf{e}_x + \frac{\partial}{\partial y}\mathbf{e}_y$. To determine the threshold of the instability, we perform linear stability analysis over the fully turbulent 2D base state. The base turbulent flow is first integrated over a few viscous timescales to reach a statistically steady state. We compute the nondimensional parameters Re, Rh, and Ro from the r.m.s. velocity ($\mathbf{u_{2D}}$) obtained from the statistically steady 2D base flow. Then the equations of perturbations (9) are solved along with the time-varying two-dimensional base flow [Eq. (5)]; these equations are also integrated up to a few viscous timescales to study the stability properties. The exponential growth or decay of the perturbations determines the threshold of the instability. Numerical integration is carried out using pseudospectral methods on a periodic domain in two dimensions. The field variables are decomposed in Fourier basis and discretized on (N, N) grid points along the x and y directions. Time marching is done using the ARS443 scheme, a four-step third-order Runge-Kutta scheme.

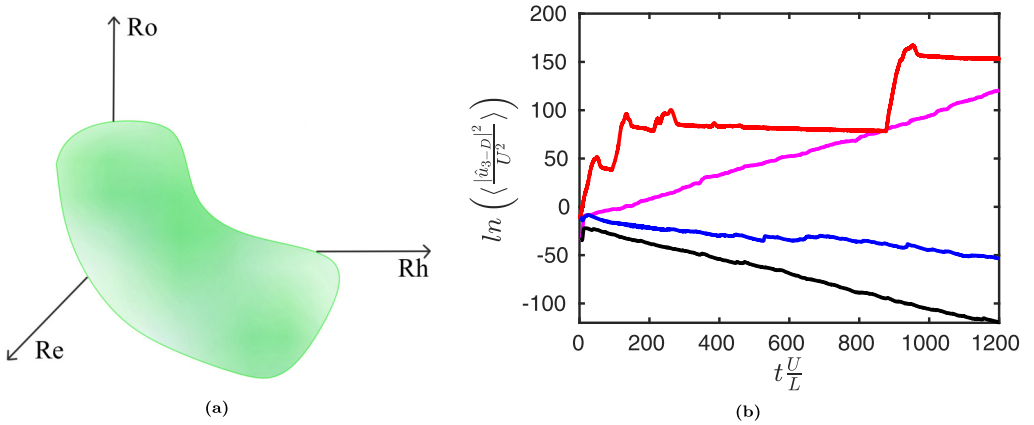

FIG. 1. Panel (a) shows a representation of the instability threshold Ro_c as a function of both Rh and Re. Above this curve the two-dimensional flow is unstable to infinitesimal 3D perturbations, while below this curve it is stable. Panel (b) shows the time series of the perturbation energy in a log-linear scale for different parameters: the red and magenta curves correspond to $\mathrm{Rh} = 10^5$, $\mathrm{Ro} = 2.1 \times 10^{-4}$ and $\mathrm{Rh} = 1$, $\mathrm{Ro} = 2.9 \times 10^{-3}$, respectively, showing the growth of perturbation while the blue and black curve corresponds to $\mathrm{Rh} = 1$, $\mathrm{Ro} = 1.6 \times 10^{-3}$ and $\mathrm{Rh} = 10$, $\mathrm{Ro} = 1.3 \times 10^{-3}$, respectively, showing decay of perturbations. The Reynolds number is fixed at $\mathrm{Re} = 10^5$ and domain size at $qL = 2\pi/10$ for all the curves.

III. RESULTS

A. Dependence on Re and Rh

We study the domains of stability in terms of the Rossby numbers Ro as a function of the parameters Re, Rh for a given aspect ratio qL, illustrated in Fig. 1(a). Figure 1(b) shows the time series of the perturbation energy in a log-linear scale for different values of Rh, Ro. As can be seen from the figure, the growth is intermittent, and the flow is considered unstable if the perturbation energy grows over the domain of integration, while it is considered stable if the perturbations decay over the entire integration time. The simulations are run up to viscous timescales to account for the evolution over very long timescales.

Figure 2(a) shows the onset as a function of Re and domain size qL at constant Rh. Due to the intermittent nature of the growth of the perturbations, the exact threshold is difficult to quantify. Therefore, we find the stable and unstable Ro values away from the threshold, the two points being the end points of the horizontal lines shown in the figure and for visualization purpose, we denote the threshold by a marker at their average. Those points marked by filled symbols correspond to the instability driven by the centrifugal instability while nonfilled symbols correspond to the parametric instability. We study the threshold Ro_c for five different aspect ratios, $qL = 2\pi L/H = 2\pi/10,\ 6\pi/10,\ 2\pi,\ 6\pi,\ 20\pi$ with the aspect ratio of $qL = 2\pi$ corresponds to a box of equal height and length, $qL = 2\pi/10,\ 6\pi/10$ correspond to vertically elongated boxes with a larger height than length while $qL = 6\pi,\ 20\pi$ correspond to thin layers with smaller height than length. As observed in Ref. [19], we find the centrifugal instability at low Re and large Ro, while for large Re and low Ro we find the parametric instability. The different scaling of the threshold distinguishes the two instabilities and whether they are seen only on the contrarotating vortex (centrifugal) or on top of both corotating and contrarotating vortices (parametric). For elongated boxes $qL = 2\pi/10$, the parametric instability is observed from lower Re numbers. At the lowest values of Re, the thresholds are governed by the centrifugal instability, further reduction in Re we find that the two-dimensional laminar flow is stable for any rotation rate shown in the figure as dashed lines. A dashed line indicating a scaling of Ro^{-1} is shown for comparison in the Fig. 2(a), the parametric instability threshold seems to follow such a scaling at large Re, simulations at even larger Re will be able to determine the validity of the scalings.

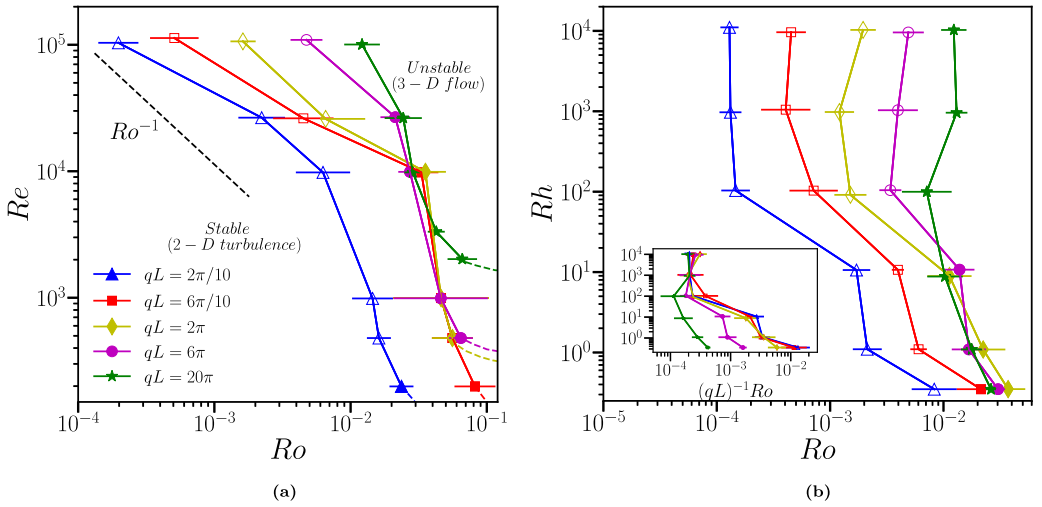

FIG. 2. Panel (a) shows the instability threshold Ro_c in the Re-Ro plane for different aspect ratios qL. The large-scale Reynolds number is fixed at $\mathrm{Rh} = 9.4 \times 10^4$ for all the curves. (b) shows the instability threshold Ro_c in the Rh-Ro plane for different aspect ratios qL. Here the Reynolds number is fixed at $\mathrm{Re} = 1.0 \times 10^5$ for all the curves. The inset in panel (b) shows the threshold with a rescaled x axis given by $(q\,L)^{-1}\mathrm{Ro}$. The dashed lines in panel (a) corresponds to the scaling law $\mathrm{Ro}_c \sim \mathrm{Re}^{-1}$ shown for comparison.

Figure 2(b) shows the threshold Ro_c as a function of the large-scale Reynolds number Rh for different aspect ratios $q\,L$ at $\mathrm{Re} = 1.0 \times 10^5$, where the filled and nonfilled symbols denote centrifugal and parametric type instabilities. Re is kept constant by varying the forcing as the large-scale dissipation affects the energy content in the two-dimensional turbulent flow. For the centrifugal instability points, the threshold Ro_c remains almost constant for a wide range of Rh explored in this study while for the parametric type instability, there is a dependence on Rh. In the large Re regime, we find that for large values of Rh, above $\mathrm{Rh} \gtrsim 10^2$, there is no effect of large-scale dissipation on the threshold, while for smaller values of $\mathrm{Rh} \lesssim 10^2$ the threshold Ro_c increases with increasing dissipation rate. Keeping the dissipation effects only in the three-dimensional perturbations and assuming an amplification rate $\sim U/L$ for a given Re, one would get a critical Rh_c independent of Ro, which is not observed. It is known that the large-scale friction breaks down large vortices into smaller ones as one reduces Rh, which could modify the stability properties of the underlying turbulent flow, leading to the observed dependency of Ro_c versus Rh. The inset of Fig. 2(b) shows the threshold with the rescaled Rossby number given by $(q\,L)^{-1}\mathrm{Ro}$ for a given Re. It is to be noted that the rescaling collapses the curves for the parametric instability points, while for the centrifugal instability points the threshold is independent of the nondimensional vertical wave number $q\,L$. Figure 3 shows the influence of Re on the threshold curves obtained in the Ro-Rh plane with Fig. 3(a) corresponding to the case of $q\,L = 2\pi$ and Fig. 3(b) to the case of $q\,L = 2\pi/10$. With increasing Re, we see the curves shifting to smaller Ro, and the threshold becomes independent of Rh for $\mathrm{Rh} \gtrsim 10^2$. For a given aspect ratio qL, the predominant instability mechanism at large Re, Rh is the parametric instability, increasing either the large-scale friction or the viscosity results in the centrifugal instability being the dominant mechanism. For very elongated boxes, $qL \ll 1$, we find that the parametric instability as the destabilization mechanism for the two-dimensional turbulent flow across a wide range of Re-Rh.

B. Instability length scales

We aim to further our understanding of the threshold by quantifying the length scales of the unstable mode. Centrifugal instability has a threshold given by a critical Ro that is almost

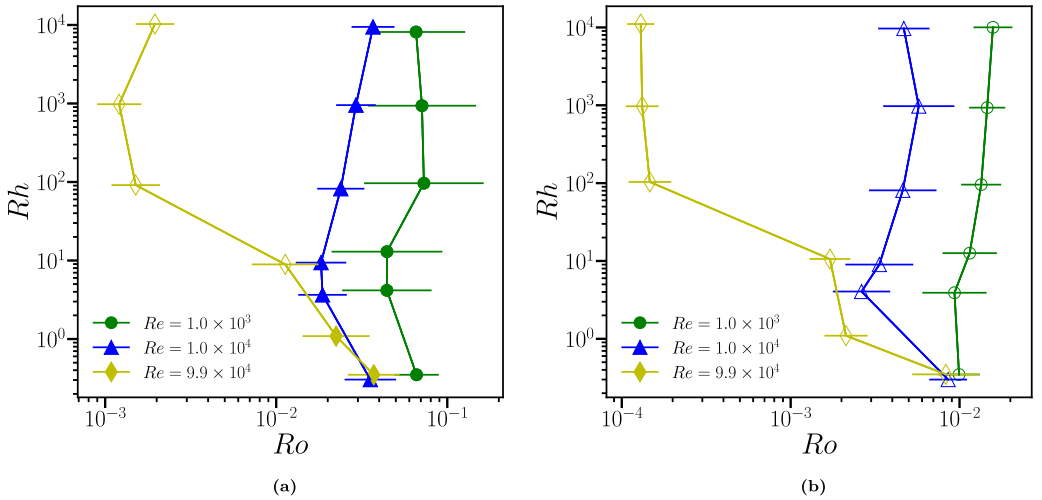

FIG. 3. The figures show the dependence of the threshold Ro_c curves as a function of the large-scale friction Rh with panel (a) corresponding to an aspect ratio $q\,L = 2\pi$ and panel (b) to an aspect ratio $q\,L = 2\pi/10$. The different curves correspond to different Re. Filled symbols correspond to centrifugal instability mechanism, while nonfilled symbols denote the parametric instability points.

independent of the Re and Rh. While the parametric instability has a threshold Ro_c that depends on both Re and Rh. Figures 4(a) and 4(b) show the real part of the x component of the vorticity field of the perturbation $\hat{\omega}_x^r$ centered at (0.5,0.5) at an instant in time when the perturbations are exponentially growing, thus denoting the unstable mode. Figure 4(a) corresponds to the parametric instability while Fig. 4(b) corresponds to the centrifugal instability. The parameters for the simulation shown in Fig. 4(a) are $qL = 2\pi$, $\mathrm{Re} = 1.1 \times 10^5$, $\mathrm{Rh} = 1.2 \times 10^5$ and those for Fig. 4(b) are $qL = 20\pi$, $\mathrm{Re} = 1.0 \times 10^5$, $\mathrm{Rh} = 1.1 \times 10^5$. The parametric instability shows a layered structure of alternating signs of three-dimensional vorticity as one goes radially away from the center of the underlying vortex, whereas the centrifugal instability shows fewer variations and is seen to be concentrated away from the center of the underlying two-dimensional contrarotating vortex. The azimuthal variation for the centrifugal instability resembles the $m = 1$ mode, while the parametric instability has a $m = 2$ mode structure. Figure 4(c) shows the real part of vorticity field $\hat{\omega}_x^r$ profile

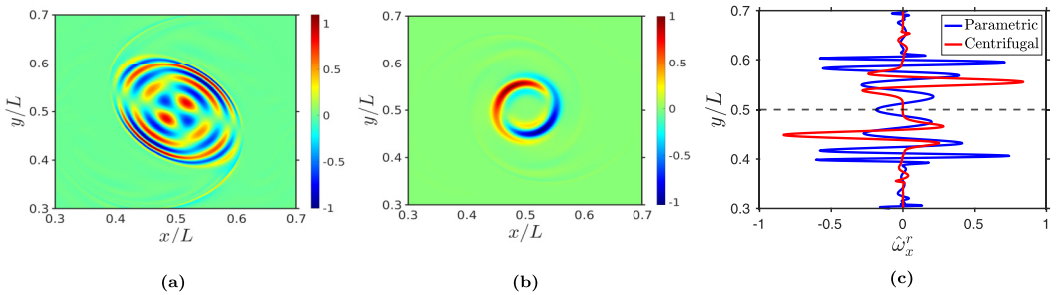

FIG. 4. The real part of x component of 3D-perturbation vorticity field is shown in panel (a) for moderate domain ($q\,L = 2\pi$) corresponding to $\mathrm{Re} = 1.1 \times 10^5$, $\mathrm{Rh} = 1.2 \times 10^5$, in panel (b) for thinner domain ($q\,L = 20\pi$) corresponding to $\mathrm{Re} = 1.0 \times 10^5$, $\mathrm{Rh} = 1.1 \times 10^5$. Panel (c) shows the variation of the real part of the x component of the vorticity at the mid-x plane ($x/L = 0.5$) as a function of y. The blue curve shows the profile corresponding to the parametric instability and the red curve shows the profile for the centrifugal instability.

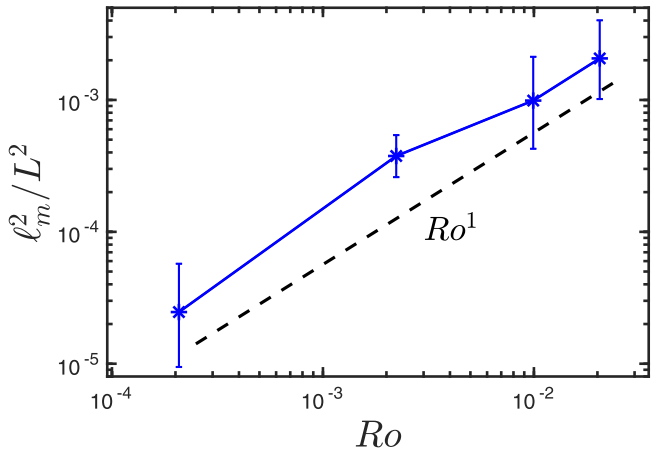

FIG. 5. Shows the variation of the length scale of the unstable mode ℓ_m as a function of the critical Rossby number Ro_c for the points associated with parametric instability. The data is obtained for the parameters corresponding to $qL = 2\pi/10$, $\mathrm{Rh} = 9.4 \times 10^4$, and varying Re. The dashed line with a scaling Ro^1 is shown for comparison.

along the midplane $x = 0$ for both the snapshots in Figs. 4(a) and 4(b). We find that the unstable mode for the centrifugal instability is antisymmetric about the y midplane, while the parametric instability shows symmetric distribution about the y midplane close to the center of the vortex, having the symmetries of the $m = 1$ and $m = 2$ mode structure respectively. Given the structure of the unstable mode, we analyze the length scales at which the instabilities in the turbulent flow are triggered. We define a length scale ℓ_m of the three-dimensional perturbation velocity fields as

$$\frac{\ell_m^2}{L^2} = \frac{1}{L^2}\frac{\langle|\hat{v}|^2\rangle}{\langle|\nabla\hat{v}|^2\rangle}. \tag{10}$$

Figure 5 shows the nondimensional square of the length scale, ℓ_m^2/L^2 as a function of the Ro number for the parameters $qL = 2\pi/10$, $\mathrm{Rh} = 9.4 \times 10^4$ for varying Re, all the points correspond to the parametric instability. As seen from the figure we find that the typical length scale of the unstable mode ℓ_m^2 to scale like Ro for almost two decades of variation in Ro. Thus, as the Ro goes to zero, the length scale for the perturbation due to the parametric instability also goes to zero. Taking the typical growth rates to scale as the turnover rate U/L and the dissipation rate to scale as $\nu\ell_m^{-2}$, balancing the two gives the observed scaling $\mathrm{Ro}_c \sim \mathrm{Re}^{-1}$. For the centrifugal instability, we find that the length scale of the unstable mode is almost constant for varying Re. Thus, the length scale of the unstable mode controls the threshold Ro_c dependence on Re.

C. Correlation with strain rate tensor

While the length scales help us to understand the scaling relation $\mathrm{Ro}_c \sim \mathrm{Re}^{-1}$, the exact onset of the parametric instability is not known. In the case of centrifugal instability, the minimum vorticity is found to be correlated with the growth rates, with the threshold given by the Rayleigh criterion [19]. For the parametric instability, no such criterion is known, as the growth rate is not directly correlated with fluctuations of the underlying vorticity field. We find that the parametric instability occurs on both the corotating and contrarotating vortices similar to elliptical type instability, which occurs on sheared vortices [31,32]. To explore this further, we aim to quantify the correlation between the growth rate and the underlying strain field of the two-dimensional turbulent flow. The strain rate tensor is defined as $S_{ij} = (\partial_i u_j + \partial_j u_i)/2$, and the quantities which are invariant under rotations of the coordinates are the trace and the determinant of the tensor. The trace of

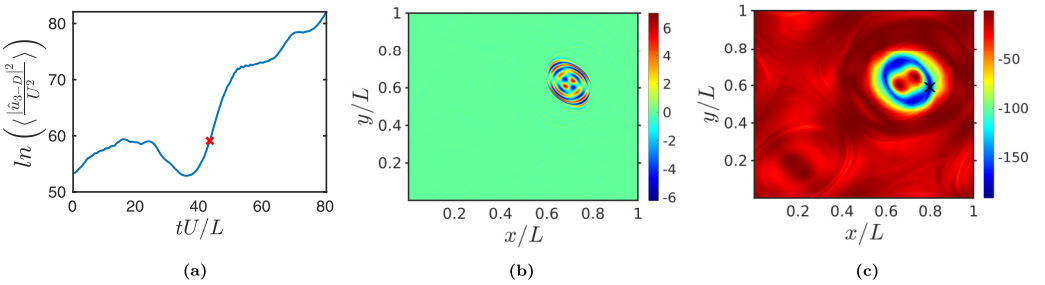

FIG. 6. Panel (a) shows the time series of the logarithm of the perturbation energy for the parameters $\mathrm{Re} = 1.1 \times 10^5$, $\mathrm{Rh} = 1.2 \times 10^5$, $\mathrm{Ro} = 1.6 \times 10^{-3}$, and $qL = 2\pi$. The cross symbol on the figure denotes the time instant at which panels (b) and (c) are taken, panel (b) shows the real part of the x component of vorticity $\hat{\omega}_x^r$ of 3D perturbations and panel (c) shows the determinant of the strain rate tensor field for the underlying two-dimensional turbulent flow S_{det}. The black marker in panel (c) denotes the position of the minimum of the determinant of the strain rate tensor.

the strain rate tensor is given by the incompressibility condition, thus it is always zero, while the determinant of the strain rate tensor is given by $S_{\mathrm{det}} = -((\partial_x u)^2 + (\partial_y u + \partial_x v)^2/4)$ and is a negative definite quantity. First, we look for spatial correlation between the minimum of the strain rate tensor and the three-dimensional perturbations. Figure 6(a) shows the time series of the logarithm of the three-dimensional perturbation energy for the parameters $\mathrm{Re} = 1.1 \times 10^5$, $\mathrm{Ro} = 1.6 \times 10^{-3}$, $\mathrm{Rh} = 1.2 \times 10^5$, $qL = 2\pi$, a cross marker is also shown on the time series which denotes the time instant at which quantities shown in Figs. 6(b) and 6(c) are computed. Figure 6(b) shows the snapshots of the real part of the x component of the 3D vorticity perturbation $\hat{\omega}_x^r$, while Fig. 6(c) shows the determinant of the strain rate tensor field of the underlying two-dimensional turbulent flow. We see that in the time instant at which the perturbations are growing, the unstable mode is concentrated near the region of large magnitude of strain rate. The large negative strain region shown in Fig. 6(c) corresponds to the corotating vortex region centered around $(x, y) \sim (0.70, 0.62)$ while the contrarotating vortex is centered around $(x, y) \sim (0.20, 0.17)$ has a relatively smaller strain rate. As the 2D-turbulent flow evolves we find that the region of strong strain rate oscillates between the corotating and contrarotating vortex. The decay of the perturbations seen in Fig. 6(a) results from the spatial decorrelation between the three-dimensional perturbations and the region of strong shear. This occurs when the strain rate on the corotating vortex reduces and the region of large strain rate is found to occur on the contrarotating vortex. The instability grows either on the corotating or on the contrarotating vortex depending on whether the local rate of strain is large. A similar correlation is also seen for the other data points where the parametric excitation mechanism is present on top of large vortices, with the growth phase of the instability is seen when the localised rate of strain is large, along with a spatial correlation between the unstable mode and the region of the strong strain rate.

To determine the temporal correlation between the rate of strain tensor and the growth rate of perturbations, we find the minimum of the determinant of the strain rate tensor defined as

$$S_{\mathrm{det}}^{\mathrm{min}}(t) = \min_{x,y} S_{\mathrm{det}}(x, y, t). \tag{11}$$

In the growth phase, the instability is found in the region of strong strain rate where the minima of the determinant of the rate of strain is also located. This is seen in Fig. 6(c), where the cross symbol denotes the location of the minima of S_{det}. Figure 7 shows the correlation of the growth rate of the unstable mode with the minimum of the determinant of the rate of strain tensor normalized with the square of the turnover time $S_{\mathrm{det}}^{\mathrm{min}} L^2/U^2$ for different values of Ro number at $\mathrm{Re} = 1.1 \times 10^5$, $\mathrm{Rh} = 1.2 \times 10^5$. The curves with circle symbols correspond to higher Ro leading to an instability, while those with square symbols correspond to lower Ro leading to a stable flow. As one increases

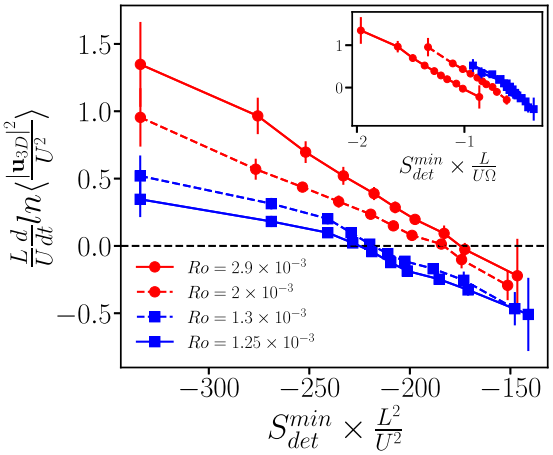

FIG. 7. Shows the scatter plot of the minimum of the determinant of the strain rate tensor $[S^{\min}_{\det}(x, y)]$ plotted against the growth rate of 3D perturbation for $\mathrm{Re} = 1.1 \times 10^5$, $\mathrm{Rh} = 1.2 \times 10^5$ and $qL = 2\pi$. Inset shows the same plot with a rescaled strain rate given by $S^{\min}_{\det}(x, y) \times [L/(U\Omega)]$.

Ro, we see that the correlation curves shift upwards, making the flow unstable to 3D perturbation for a larger range of $S^{\min}_{\det}(x, y)$. The inset shows the growth rate values at different values of the minimum determinant of the rate of strain normalized with $L/(U\Omega)$. This normalization factor is chosen since it scales the minimum of the rate of strain tensor with the rotation rate and the turnover timescale, as one would expect from the threshold scaling $\mathrm{Re} \times \mathrm{Ro} \sim$ const. While this leads to a criterion of $S^{\min}_{\det} L/(U\Omega) = \alpha \lesssim O(1)$ below which the system is unstable, the normalization does not rescale all the curves on top of each other. The exact value of α will depend on other parameters such as qL, Re, local vorticity and rate of strain. In the case of elliptical instabilities, where weakly strained vortices are destabilized [31–33], it is found that the growth rate is proportional to the strain rate imposed on these vortices with the linearity being valid when the rate of strain is small compared to the vorticity. For strongly strained vortices, an analytical relation between the growth rate of perturbations and the rate of strain is unknown. While studies on elliptical instabilities consider a stationary strained vortex, here the presence of fluctuations is important in triggering the parametric instability. Elliptical instabilities of a vortex subjected to an external strain, with time dependency imposed on either the vortex or the strain have also been studied [34–36], though an analytical criterion for the threshold remained unknown.

IV. OSCILLATORY KOLMOGOROV FLOW

The previous sections have helped us understand the nature of the parametric instability seen on top of rapidly rotating two-dimensional flows. Given the difficulty in understanding the instability process on the turbulent background and the absence of an exact threshold, we look to a simpler model to study the parametric instability. The destabilization of an oscillating flow was proposed as a model in Ref. [19], which took into account the time dependence and reproduced the Reynolds number dependence of the threshold Ro_c. Here, we look at the destabilization of the oscillating Kolmogorov flow to understand the influence of large-scale friction, aspect ratio and the oscillation frequency on the threshold of the instability. The oscillatory Kolmogorov flow used in this study is given by $\mathbf{u} = 2\,U\,\cos(4\pi y/L)\cos(4\pi\,\chi\,t\,U/L)\mathbf{e}_x$ where χ is a nondimensional parameter that indicates the strength of the oscillation frequency in units of the inverse turnover timescale U/L. The stability of the oscillatory Kolmogorov flow subject to global rotation is studied using a numerical code based on Floquet theory. We look at the instability threshold in the presence of a large-scale friction term and we take the underlying flow amplitude to be fixed, thus the friction only affects the

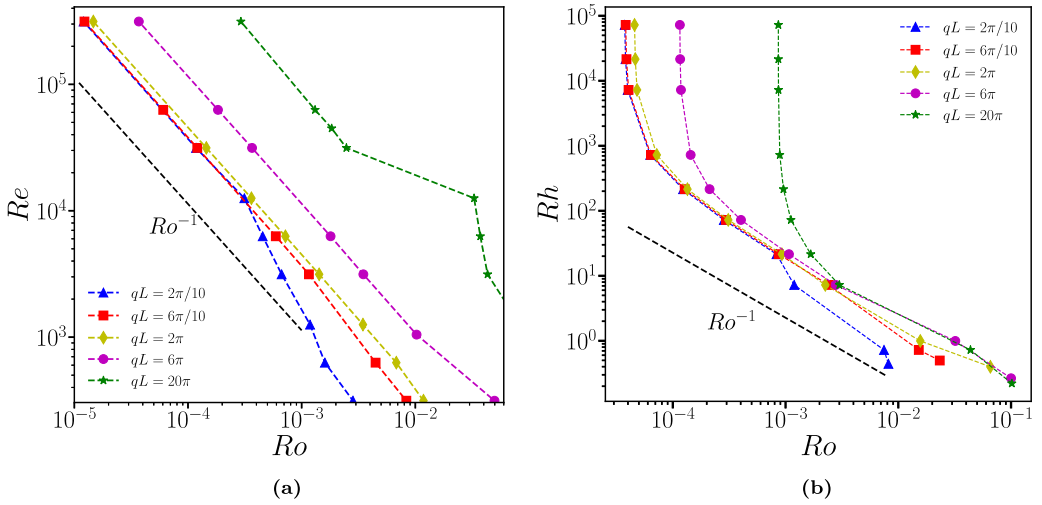

FIG. 8. Figures show the threshold Ro_c as a function of the Reynolds numbers Re, Rh, for the oscillatory Kolmogorov flow for different aspect ratios qL. Parameter corresponding to panel (a) Re vs Ro is $\mathrm{Rh} = 1.0 \times 10^5$ and panel (b) Rh vs Ro is $\mathrm{Re} = 1.0 \times 10^5$.

evolution of the perturbations. Initially, we fix $\chi = 1$ and show in Fig. 8(a) the instability threshold in the Re-Ro plane for different aspect ratios that we considered in the problem. For these points, the large-scale friction is kept very small $\mathrm{Rh} \sim 10^5$. We see that for $qL = 2\pi$, the threshold is given by $\mathrm{Ro}_c \sim \mathrm{Re}^{-1}$ at large values of Re. For thinner domains (larger $qL = 20\pi$) the threshold for small Re is almost independent of the Re, while for larger Re the threshold scales as $\mathrm{Ro}_c \sim \mathrm{Re}^{-1}$. At very large values of Re, all the curves for different qL asymptote to a threshold which scales with the Reynolds number as $\mathrm{Ro}_c \sim \mathrm{Re}^{-1}$. Comparing with the turbulent 2D flows, we also find a change in the scaling behavior as one increases Re see Fig. 2(a), but this occurs due to a change in the dominant instability mechanism from the centrifugal instability to the parametric instability as one changes Re. A difference is also observed in the dependence of the threshold on qL, wherein the turbulent case we have a rescaling going as $\mathrm{Ro}_c \sim (qL)$, which is not observed for the oscillating Kolmogorov flows.

Figure 8(b) shows the dependence of the threshold on the large-scale friction threshold Ro_c in the Rh-Ro plane for the case $\mathrm{Re} = 1.0 \times 10^5$. For large Rh, the threshold asymptotes to the friction-independent value agreeing with the values from Fig. 8(a), while for small Rh we see that the threshold increases as Rh decreases due to stronger dissipation. Since the friction is present only in the perturbation equation, we find that the threshold follows the scaling of $\mathrm{Ro}_c \sim \mathrm{Rh}^{-1}$ when the large-scale dissipation is strong, this scaling is obtained by balancing the growth rate $(U/L)\,\mathrm{Ro}$ with the dissipation rate μ. It is to be noted that the growth rate in the case of the oscillating Kolmogorov flow is proportional to the Rossby number as the formation of the three-dimensional mode is through quartic interactions [24] or quasi-resonances [37]. Similar to Fig. 8(a), we find that the dependence on qL differs from the turbulent case. To understand the relation between the threshold and the aspect ratio, we show in Fig. 9(a) the threshold Ro_c as a function of qL for three different values of Re, Rh. While the case of smaller Rh, Re show a scaling for the threshold $\mathrm{Ro}_c \sim qL$, the larger values show deviation from this scaling. The deviation from the scaling is seen due to the occurrence of a large-scale unstable mode, which is the dominant mode when the large-scale friction is small.

Next we look at the influence of the nondimensional oscillation frequency χ on the onset of the instability. Figure 9(b) shows the instability threshold for three different values of χ for $qL = 2\pi/10$, $\mathrm{Rh} = 1.0 \times 10^5$. As the frequency is increased, we see that the threshold shifts to smaller values of Ro, this occurs since the available range of inertial waves that can be excited increases

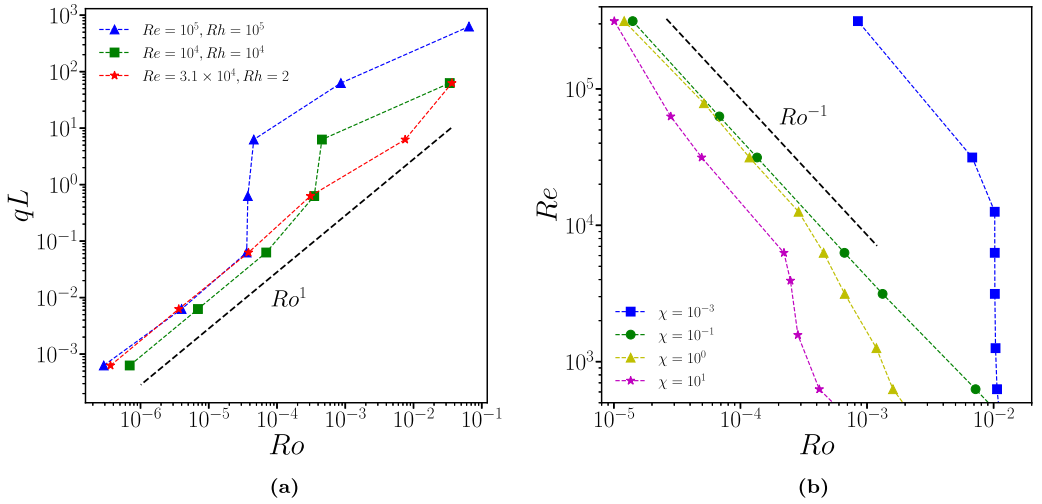

FIG. 9. Figures show the dependence of the threshold Ro_c on the aspect ratio qL in panel (a) and the oscillation frequency χ in panel (b) for the oscillatory Kolmogorov flow. The dashed lines indicate a scaling Ro^1 in panel (a) and Ro^{-1} in panel (b), are shown for comparison. In panel (b) the threshold Ro_c is obtained for the parameters $q\,L = 2\pi/10$ and $\mathrm{Rh} = 1.0 \times 10^5$.

with increasing frequency of oscillation. At large Re the threshold asymptotes to the Re^{-1} behavior for all the frequencies shown. When the oscillation frequency is minimal compared to the turnover frequency $\chi \ll 1$, the instability threshold is independent of Re for intermediate values of Re while for large values of Re the threshold asymptotes to a $\mathrm{Ro}_c \sim \mathrm{Re}^{-1}$ scaling. The limiting case of $\chi = 0$ leads to the stationary Kolmogorov flow which has a threshold of $\mathrm{Ro}_c \approx 0.056$. We find that the oscillation frequency of the underlying flow strongly affects the threshold Ro_c of the instability.

We find that the destabilization of the rapidly rotating oscillatory Kolmogorov flow predicts the scaling of $\mathrm{Ro}_c \sim \mathrm{Rh}^{-1}$ when the large-scale friction effect is strong, and the scaling $\mathrm{Ro}_c \sim \mathrm{Re}^{-1}$ at large Re. While the dependency on the dissipation coefficients can be understood by balancing the growth rate with the dissipation rates, the dependence on the aspect ratio and oscillation frequency is less understood.

V. CONCLUSIONS

Modeling the effect of confinement as a large-scale friction term we have studied the linear instability threshold of three-dimensional perturbations on a rapidly rotating two-dimensional turbulent flow. The large-scale drag term shifts the threshold to larger values of the Ro number, when the instability mechanism is parametric. While for the centrifugal type instability found at lower Re, the friction term for the parameter range explored in this study does not affect the threshold. For the oscillating Kolmogorov flow destabilization by the parametric instability, the large-scale friction affected only the perturbation equations leading to a scaling of $\mathrm{Ro}_c \sim \mathrm{Rh}^{-1}$. While in the turbulent flow, there is a deviation from this scaling as the friction breaks down large-scale vortices into smaller ones, affecting their stability properties. This study used the linear friction to model the dissipation effects from the Ekman layers (see the Appendix). Future studies can incorporate the effect of a quadratic drag term which is applicable when the Ekman boundary layer becomes turbulent. The presence of side walls is also not considered in this study, they can induce Ekman pumping [1,38] from which a vertical component of the velocity field is induced. The modification from the Ekman pumping is expected to be smaller in magnitude as compared to the two-dimensional velocity field components which are directly forced. Nevertheless, a study

on the effect of both vertical and horizontal boundaries in the limit of very low Rossby numbers can shed light upon the onset of three-dimensional perturbations that destablize the columnar vortices.

We have seen two different instability mechanisms: centrifugal and parametric type instabilities and have observed several ways of distinguishing between the two. Based on the spatial correlation, the unstable mode originates only inside contrarotating vortices for the case of centrifugal instability while points corresponding to parametric type instability, an unstable mode can develop inside either of the vortices [19]. In the case of parametric type instability, the unstable mode is centered around the minimum of the determinant of the strain rate tensor (see Fig. 6). In contrast, the unstable mode for the centrifugal instability is localised around the contrarotating vortex. Based on the temporal correlation, it is found that whenever the Rayleigh parameter ($[\overline{\min_x \omega_{2D}} + 2\Omega]/2\Omega$ becomes less than zero, instantaneous perturbation energy grows in the case of centrifugal instability. In the case of parametric type instability, the growth rate is correlated with a minimum of the determinant of strain rate tensor; see Fig. 7. We have checked for various data points and observed that in the case of steady flow (when the 2D base flow is frozen), instability grows for the centrifugal case but ceases to grow for parametric type instability, which shows the time-dependent nature of the latter.

In the parametric type instability, the threshold is controlled by the length scale of the unstable mode, which is found to depend on the Rossby number as $\mathrm{Ro}^{1/2}$, taking the growth rate to be the turnover timescale leads to the scaling $\mathrm{Re} \times \mathrm{Ro} \sim O(1)$. As the more strained vortex being prone to parametric-type instability, it shows similarities between the parametric instability found here and the elliptical instability found on strained vortices. In the turbulent regime for both the instability mechanisms: centrifugal and parametric instability, the destabilization of a rapidly rotating turbulent flow is governed by large fluctuations of the vorticity or the rate of strain tensor. Understanding the distribution of these large fluctuations [39] can help us understand the intermittency observed in the growth of the instability. Recent works have also focused upon the nature of the growth of perturbations in such systems where strong fluctuations in the underlying turbulent flow create intermittent events of growth and decay [40].

The current study has focused only on the linear threshold of the instability, and to check the validity of this one has to do three-dimensional simulations in the nonlinear regime. A recent work [41] has shown the existence of anomalous exponents in the saturation of instabilities on a turbulent background, extending the linear problem studied here into the nonlinear regime could explore whether such a phenomena is also seen in the case of rotating flows. While numerical simulations of fully three-dimensional turbulent flow at very low Ro and large Re is difficult, weakly nonlinear extensions as done elsewhere, see Ref. [17], can also be studied in future to determine the validity of the linear study. Beyond the study of rotating flows, turbulence in thin layers, in flows with a strong magnetic field and rotating-stratified flows also display the formation of large-scale condensates and one could look to understand when and how such structures are destabilized.

ACKNOWLEDGMENTS

The authors thank Dr. Vishwanath Shukla for his useful suggestions and insightful discussions. This work used the Supercomputing facility of IIT Kharagpur established under the National Supercomputing Mission (NSM), Government of India and supported by the Centre for Development of Advanced Computing (CDAC), Pune. S.K.N. thanks the Prime Minister's Research Fellows (PMRF) scheme, Ministry of Education, Government of India. C.S.L. acknowledges the MHRD, Government of India for the fellowship. The authors also acknowledge support from the Institute Scheme for Innovative Research and Development (ISIRD), IIT Kharagpur, Grants No. IIT/SRIC/ISIRD/2021-2022/03 and No. IIT/SRIC/ISIRD/2021–2022/08 and the National Supercomputing Mission Grant No. DST/NSM/R&D_HPC_Applications/2021/0.21, DST/NSM/R&D HPC Applications/2021/03.11 for computing facilities, and the Startup Research

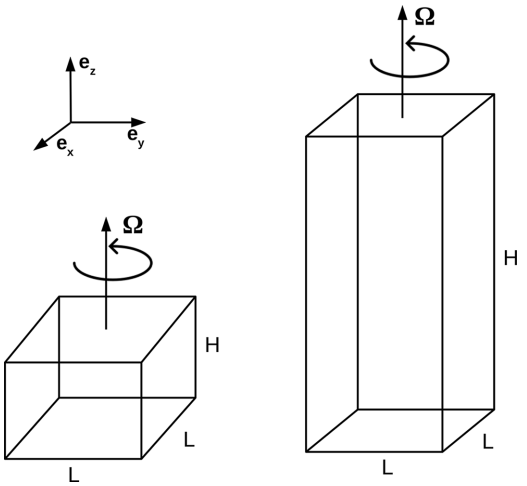

FIG. 10. Schematic showing the thinner (left) and elongated (right) domains and axis of rotation.

Grant No. SRG/2021/001229 from the department of Science and Technology (DST), Science & Engineering Research Board (SERB), India.

APPENDIX: MODELING THE EFFECT OF EKMAN LAYERS AND CONFINEMENT

Large scale friction is used to model the effect of rigid walls at $z = 0, H$. The friction coefficient μ can be estimated in terms of the parameters ν, Ω and the height H for laminar boundary layers as $\mu \sim \nu/\delta^2$. Here $\delta \sim \sqrt{\nu/\Omega}$ is given by the width of the Ekman boundary layer [1,22,42]. We consider the Navier Stokes equations in the rotating frame and decompose the flow fields in terms of the boundary contribution and interior contribution. The velocity field is then written as $\mathbf{u} = \mathbf{u}^i + \mathbf{u}^b$ as a combination of the solution from the interior denoted by $\mathbf{u}^i$ and the solution near the boundaries $\mathbf{u}^b$. The top and bottom rigid boundaries at $z = 0, H$ give rise to the condition of no-slip velocity fields $\mathbf{u} = 0$, leading to the boundary layers where the velocity field $\mathbf{u}^b$ is nonzero. We make the following assumptions, (1) that the boundary layers remain laminar, (2) we take the velocity field induced by the boundary $\mathbf{u}^b$ to go to zero outside the boundary layer, and (3) we assume that the velocity field in the interior obeys stress-free boundary conditions at the edge of the boundary layers, beyond a distance $c\sqrt{\nu/\Omega}$. Here c is a constant denoting the typical width of the boundary layer in units of $\sqrt{\nu/\Omega}$. Under these assumptions, we derive the governing equations for the interior velocity field. A schematic of the domain is shown in Fig. 10, where the boundaries of the domain are periodic along x and y directions.

1. Two-dimensional velocity field

We rescale the governing equations, Eqs. (1) and (2), near the top and bottom boundaries as, $\tilde{x} = x/L, \tilde{y} = y/L, \tilde{z} = z/\delta, \tilde{\mathbf{u}} = \mathbf{u}/U, \tilde{t} = t2\Omega$ and $\tilde{p} = p/(\rho U^2)$, here $\delta = \sqrt{\nu/\Omega}$. For small viscosity and large rotation rates, the dominant terms of the equation are given by

$$\partial_{\tilde{t}}\tilde{\mathbf{u}} = -\nabla\tilde{p} + \partial_{\tilde{z}}^2\tilde{\mathbf{u}} + \tilde{\mathbf{u}} \times \mathbf{e}_{\tilde{z}}. \tag{A1}$$

We decompose the fields into the boundary contribution (superscript b) and interior contribution (superscript i). We impose the boundary conditions: $\tilde{\mathbf{u}} = \tilde{\mathbf{u}}^i + \tilde{\mathbf{u}}^b = 0$ at $\tilde{z} = 0, H/\delta$ with the boundary contribution decaying to zero as we move away from the walls. The stationary solutions of Eq. (A1) are given by the Ekman spirals, whose solutions are given by

$$\tilde{\mathbf{u}} = \tilde{\mathbf{u}}^i + e^{\tilde{z}-H/\delta}\mathbf{F}(\tilde{x}, \tilde{y}, \tilde{z}, t) + e^{-\tilde{z}}\mathbf{G}(\tilde{x}, \tilde{y}, \tilde{z}, t). \tag{A2}$$

Here $\mathbf{F}$ and $\mathbf{G}$ contain the oscillatory variation along $\mathbf{e}_{\tilde{z}}$ denoting the Ekman spiral and they are set by the boundary conditions at $z = 0, H/\delta$.

Away from the boundaries, nondimensionalization along $\mathbf{e}_{\tilde{z}}$ can be done by L in place of δ, and $\tilde{t} = (U/L)t$; the resulting equation after substituting the expression of $\tilde{\mathbf{u}}$, we get

$$\frac{\partial \tilde{\mathbf{u}}^i}{\partial \tilde{t}} + (\tilde{\mathbf{u}}^i \cdot \boldsymbol{\nabla})\tilde{\mathbf{u}}^i = -\boldsymbol{\nabla} p + \frac{1}{\mathrm{Re}}\nabla^2 \tilde{\mathbf{u}}^i + \frac{1}{\mathrm{Ro}}(\tilde{\mathbf{u}}^i \times \mathbf{e}_{\tilde{z}}) + \mathbf{f_{2D}} + \frac{1}{\mathrm{Re}}\frac{\partial^2 \tilde{\mathbf{u}}^b}{\partial \tilde{z}^2} + \frac{1}{\mathrm{Ro}}(\tilde{\mathbf{u}}^b \times \mathbf{e}_{\tilde{z}}) - (\tilde{\mathbf{u}}^i \cdot \boldsymbol{\nabla})\tilde{\mathbf{u}}^b - (\tilde{\mathbf{u}}^b \cdot \boldsymbol{\nabla})\tilde{\mathbf{u}}^i - (\tilde{\mathbf{u}}^b \cdot \boldsymbol{\nabla})\tilde{\mathbf{u}}^b. \tag{A3}$$

We can expand $\tilde{\mathbf{u}}^i$, $\tilde{\mathbf{u}}^b$, and p as follows:

$$\tilde{\mathbf{u}}^i(\tilde{\mathbf{x}}, \tilde{t}) = \tilde{\mathbf{u}}^i_{\mathbf{2D}}(\tilde{\mathbf{x}}, \tilde{t}) + \mathrm{Ro}\, \tilde{\mathbf{u}}^i_{\mathbf{3D}}(\tilde{\mathbf{x}}, \tilde{t}) + O(\mathrm{Ro}^2), \tag{A4}$$

$$\tilde{\mathbf{u}}^b(\tilde{\mathbf{x}}, \tilde{t}) = \tilde{\mathbf{u}}^b_{\mathbf{2D}}(\tilde{\mathbf{x}}, \tilde{t}) + \mathrm{Ro}\, \tilde{\mathbf{u}}^b_{\mathbf{3D}}(\tilde{\mathbf{x}}, \tilde{t}) + O(\mathrm{Ro}^2), \tag{A5}$$

$$p(\tilde{\mathbf{x}}, \tilde{t}) = \mathrm{Ro}^{-1}\tilde{p}_G(\tilde{\mathbf{x}}, \tilde{t}) + \tilde{p}_{2\mathrm{D}}(\tilde{\mathbf{x}}, \tilde{t}) + \mathrm{Ro}\, \tilde{p}_{3\mathrm{D}}(\tilde{\mathbf{x}}, \tilde{t}) + O(\mathrm{Ro}^2). \tag{A6}$$

Using Eqs. (A4), (A5), and (A6) in Eq. (A3) and then taking average along $\mathbf{e}_{\tilde{z}}$, at order Ro^0:

$$\frac{\partial \tilde{\mathbf{u}}^i_{\mathbf{2D}}}{\partial \tilde{t}} + (\tilde{\mathbf{u}}^i_{\mathbf{2D}}.\boldsymbol{\nabla})\tilde{\mathbf{u}}^i_{\mathbf{2D}} = -\boldsymbol{\nabla}\tilde{p}_{2\mathrm{D}} + \frac{1}{\mathrm{Re}}\nabla^2 \tilde{\mathbf{u}}^i_{\mathbf{2D}} + \mathbf{f_{2D}} + \frac{1}{\mathrm{Re}}\frac{\partial \tilde{\mathbf{u}}^b_{\mathbf{2D}}}{\partial \tilde{z}}\Bigg|_{\tilde{z}=0}^{\tilde{z}=H/L}. \tag{A7}$$

We have neglected all other terms as they are proportional to the width of the boundary layer and are negligible. Leading contributions coming from the boundaries can be written in a single term $1/\mathrm{Rh}\tilde{\mathbf{u}}^{\mathbf{i}}_{\mathbf{2D}}$ where $1/\mathrm{Rh}$ is the nondimensional Reynolds number constructed from the large scale friction μ. By writing the above equation in dimensional form and dropping the superscript, we get Eq. (5).

2. Three-dimensional velocity field

The three-dimensional perturbations $\tilde{\mathbf{u}}^i_{\mathbf{3D}}(\tilde{\mathbf{x}}, \tilde{t})$ can be decomposed into vertical Fourier modes. The perturbation form can be written as

$$\tilde{\mathbf{u}}^i_{\mathbf{3D}}(\mathbf{x}, t) = \widehat{\mathbf{u}}^i_{\mathbf{3D}}(x, y, t)e^{iq\tilde{z}} + \widehat{\mathbf{u}}^{i*}_{\mathbf{3D}}(x, y, t)e^{-iq\tilde{z}}. \tag{A8}$$

For the perturbations induced in the interior, there is a velocity field induced in the boundary layer which is given by $\tilde{\mathbf{u}}^b_{\mathbf{3D}}(\tilde{\mathbf{x}}, \tilde{t})$. Using Eqs. (A4), (A5), (A6), and (A8) in Eq. (A3) and then comparing terms of the order Ro^1, we get the evolution equations of perturbations. Upon averaging the resultant equations along $\mathbf{e}_{\tilde{z}}$ and neglecting the subdominant terms having magnitude of the order of δ, we get Eq. (A9):

$$\frac{\partial \widehat{\mathbf{u}}^i_{\mathbf{3D}}}{\partial \tilde{t}} + \left(\tilde{\mathbf{u}}^i_{\mathbf{2D}} \cdot \boldsymbol{\nabla}_\perp\right)\widehat{\mathbf{u}}^i_{\mathbf{3D}} + \left(\widehat{\mathbf{u}}^i_{\mathbf{3D}} \cdot \boldsymbol{\nabla}_\perp\right)\tilde{\mathbf{u}}^i_{\mathbf{2D}} = -(\boldsymbol{\nabla}_\perp + iq\mathbf{e}_{\tilde{z}})\widehat{p}_{3\mathrm{D}} + \frac{1}{\mathrm{Re}}(\nabla^2_\perp - q^2)\widehat{\mathbf{u}}^i_{\mathbf{3D}} + \frac{1}{\mathrm{Ro}}\left(\widehat{\mathbf{u}}^i_{\mathbf{3D}} \times \mathbf{e}_{\tilde{z}}\right) + \frac{1}{\mathrm{Re}}\frac{\partial \tilde{\mathbf{u}}^b_{\mathbf{3D}}}{\partial \tilde{z}}\Bigg|_{\tilde{z}=0}^{\tilde{z}=H/L}. \tag{A9}$$

The last term can be approximated by a friction term that acts on the perturbation fields. In the dimensional form, above equation (without superscript) gives Eq. (9).

[1] J. Pedlosky, *Geophysical Fluid Dynamics* (Springer Science & Business Media, Berlin, 2013).

[2] D. J. Tritton, *Physical Fluid Dynamics* (Springer Science & Business Media, Berlin, 2012).
[3] G. K. Vallis, *Atmospheric and Oceanic Fluid Dynamics* (Cambridge University Press, Cambridge, UK, 2017).
[4] G. Boffetta, R. E. Ecke *et al.*, Two-dimensional turbulence, Annu. Rev. Fluid Mech. **44**, 427 (2012).
[5] A. Ibbetson and D. Tritton, Experiments on turbulence in a rotating fluid, J. Fluid Mech. **68**, 639 (1975).
[6] C. N. Baroud, B. B. Plapp, H. L. Swinney, and Z.-S. She, Scaling in three-dimensional and quasi-two-dimensional rotating turbulent flows, Phys. Fluids **15**, 2091 (2003).
[7] L. M. Smith and F. Waleffe, Transfer of energy to two-dimensional large scales in forced, rotating three-dimensional turbulence, Phys. Fluids **11**, 1608 (1999).
[8] F. Godeferd and L. Lollini, Direct numerical simulations of turbulence with confinement and rotation, J. Fluid Mech. **393**, 257 (1999).
[9] A. Alexakis, Rotating Taylor–Green flow, J. Fluid Mech. **769**, 46 (2015).
[10] N. Yokoyama and M. Takaoka, Hysteretic transitions between quasi-two-dimensional flow and three-dimensional flow in forced rotating turbulence, Phys. Rev. Fluids **2**, 092602(R) (2017).
[11] E. Deusebio, G. Boffetta, E. Lindborg, and S. Musacchio, Dimensional transition in rotating turbulence, Phys. Rev. E **90**, 023005(R) (2014).
[12] T. Pestana and S. Hickel, Regime transition in the energy cascade of rotating turbulence, Phys. Rev. E **99**, 053103 (2019).
[13] K. Seshasayanan and A. Alexakis, Condensates in rotating turbulent flows, J. Fluid Mech. **841**, 434 (2018).
[14] A. van Kan and A. Alexakis, Critical transition in fast-rotating turbulence within highly elongated domains, J. Fluid Mech. **899**, A33 (2020).
[15] A. Alexakis and L. Biferale, Cascades and transitions in turbulent flows, Phys. Rep. **767-769**, 1 (2018).
[16] A. Celani, S. Musacchio, and D. Vincenzi, Turbulence in more than two and less than three dimensions, Phys. Rev. Lett. **104**, 184506 (2010).
[17] S. J. Benavides and A. Alexakis, Critical transitions in thin layer turbulence, J. Fluid Mech. **822**, 364 (2017).
[18] B. Gallet, Exact two-dimensionalization of rapidly rotating large-Reynolds-number flows, J. Fluid Mech. **783**, 412 (2015).
[19] K. Seshasayanan and B. Gallet, Onset of three-dimensionality in rapidly rotating turbulent flows, J. Fluid Mech. **901**, R5 (2020).
[20] E. Yarom, Y. Vardi, and E. Sharon, Experimental quantification of inverse energy cascade in deep rotating turbulence, Phys. Fluids **25**, 085105 (2013).
[21] N. Machicoane, F. Moisy, and P.-P. Cortet, Two-dimensionalization of the flow driven by a slowly rotating impeller in a rapidly rotating fluid, Phys. Rev. Fluids **1**, 073701 (2016).
[22] D. Sous, J. Sommeria, and D. Boyer, Friction law and turbulent properties in a laboratory Ekman boundary layer, Phys. Fluids **25**, 046602 (2013).
[23] T. Le Reun, B. Favier, A. J. Barker, and M. Le Bars, Inertial wave turbulence driven by elliptical instability, Phys. Rev. Lett. **119**, 034502 (2017).
[24] M. Brunet, B. Gallet, and P.-P. Cortet, Shortcut to geostrophy in wave-driven rotating turbulence: The quartetic instability, Phys. Rev. Lett. **124**, 124501 (2020).
[25] L. Zavala Sansón, G. van Heijst, and N. Backx, Ekman decay of a dipolar vortex in a rotating fluid, Phys. Fluids **13**, 440 (2001).
[26] C. Morize and F. Moisy, Energy decay of rotating turbulence with confinement effects, Phys. Fluids **18**, 065107 (2006).
[27] P. Billant, Is the taylor–proudman theorem exact in unbounded domains? Case study of the three-dimensional stability of a vortex pair in a rapidly rotating fluid, J. Fluid Mech. **920**, R1 (2021).
[28] A. van Kan, A. Alexakis, and M.-E. Brachet, Intermittency of three-dimensional perturbations in a point-vortex model, Phys. Rev. E **103**, 053102 (2021).
[29] E. Monsalve, M. Brunet, B. Gallet, and P.-P. Cortet, Quantitative experimental observation of weak inertial-wave turbulence, Phys. Rev. Lett. **125**, 254502 (2020).

[30] V. M. Parfenyev and S. S. Vergeles, Influence of Ekman friction on the velocity profile of a coherent vortex in a three-dimensional rotating turbulent flow, Phys. Fluids **33**, 115128 (2021).
[31] B. Bayly, Three-dimensional instability of elliptical flow, Phys. Rev. Lett. **57**, 2160 (1986).
[32] R. R. Kerswell, Elliptical instability, Annu. Rev. Fluid Mech. **34**, 83 (2002).
[33] A. Craik, The stability of unbounded two-and three-dimensional flows subject to body forces: Some exact solutions, J. Fluid Mech. **198**, 275 (1989).
[34] A. Craik and H. Allen, The stability of three-dimensional time-periodic flows with spatially uniform strain rates, J. Fluid Mech. **234**, 613 (1992).
[35] W. F. Baylay, D. Holm, and A. Lifschitz, Three-dimensional stability of elliptical vortex columns in external strain flows, Philos. Trans. Roy. Soc. London Ser. A: Math. Phys. Eng. Sci. **354**, 895 (1996).
[36] S. Le Dizes, M. Rossi, and H. Moffatt, On the three-dimensional instability of elliptical vortex subjected to stretching, Phys. Fluids **8**, 2084 (1996).
[37] T. Le Reun, B. Gallet, B. Favier, and M. Le Bars, Near-resonant instability of geostrophic modes: Beyond Greenspan's theorem, J. Fluid Mech. **900**, R2 (2020).
[38] G. J. F. van Heijst and H. Clercx, Laboratory modeling of geophysical vortices, Annu. Rev. Fluid Mech. **41**, 143 (2009).
[39] K. Seshasayanan, Spatial extreme values of vorticity and velocity gradients in two-dimensional turbulent flows, arXiv preprint arXiv:2301.09900.
[40] A. van Kan, A. Alexakis, and M.-E. Brachet, Lévy on-off intermittency, Phys. Rev. E **103**, 052115 (2021).
[41] A. Alexakis, F. Pétrélis, S. J. Benavides, and K. Seshasayanan, Symmetry breaking in a turbulent environment, Phys. Rev. Fluids **6**, 024605 (2021).
[42] M. Lesieur, Introduction to turbulence in fluid mechanics, *Turbulence in Fluids* (Springer, Dordrecht, 2008).